

Characterization of the Atherosclerotic Plaque Tissue

Phani Kumari Paritala¹, Tejasri Yarlagadda², Jessica Benitez Mendieta¹, Jiaqiu Wang¹, YuanTong Gu¹, Zhiyong Li¹, Prasad K.D.V. Yarlagadda^{1,*}

¹School of Mechanical, Medical and Process Engineering, Queensland University of Technology, Brisbane QLD 4000, Australia

²Institute of Health Biomedical Innovation (IHBI), Faculty of Health, Queensland University of Technology, Brisbane QLD 4000, Australia

*Corresponding author: E-mail: y.prasad@qut.edu.au; Tel.: (+61) 731385167

DOI: 10.5185/amlett.2020.051507

Cardiovascular diseases (CVD) are the leading causes of morbidity and mortality globally. Atherosclerosis is a chronic inflammatory CVD associated with the accumulation of plaque activated by the complex interactions between systemic, hemodynamic and biological factors. Thus, identification of plaque vulnerability is essential for the prevention of acute events and treatment of the disease. Despite, advanced imaging technologies, patient-specific computational simulations and availability of experimental data, there are still challenges in developing accurate risk stratification techniques. Therefore, this study aims to characterize the carotid plaque components structurally (histological analysis and immunostaining), mechanically (Nanoindentation tests) and chemically (Fourier Transform Infrared (FT-IR) micro-spectroscopy). The preliminary results showed that arterial remodelling is a dynamic interaction between mechanical forces and plaque progression. The biological content and composition of human atherosclerotic plaque tissue have been shown to significantly influence the mechanical response of samples. This data represents a step towards an enhanced understanding of the behaviour of human atherosclerotic plaque. Future large-scale experimental studies with more cross-sections along the length of the plaque could be used to develop a risk stratification technique.

Introduction

Atherosclerosis, a significant cause for the majority of the cardiovascular events is a chronic inflammatory disease associated with the accumulation of plaque activated by the complex interactions between systemic, hemodynamic and biological factors [1]. These lesions result from the inflammatory-fibroproliferative response to injury of the endothelium [2]. The mechanisms involving plaque formation are lipid retention, oxidation, and modification that provokes inflammation results in thrombosis or stenosis [3]. Atherosclerotic plaque rupture in carotid arteries is the leading cause of ischemic strokes [4] that results in mortality and long-term morbidity in developed countries [5]. Plaque rupture occurs in vulnerable plaques characterized by a thin fibrous cap covering a sizeable necrotic core [6-8]. Therefore, assessment of the morphological features of the atherosclerotic plaque is essential. Several imaging modalities such as ultrasound and high-resolution magnetic resonance (MRI) [8-10] have been used to identify the morphological features of the atherosclerotic plaque in the carotid arteries. Furthermore, patient-specific computational models are often used to investigate plaque geometries susceptible to rupture [11-20]. The stresses induced in the arteries due to the hemodynamic blood flow plays an essential role in plaque mechanics. Therefore, understanding the effect of biomechanical forces on the plaque progression is essential for developing accurate imaging procedures for vulnerability assessments. Moreover, biomechanical characterization of the plaque constituents' aids in

accurate assessment of the plaque stresses. It is anticipated that patient-specific computational modeling, combined with accurate material models, will allow clinicians to identify vulnerable plaques and tailor treatments based on plaque composition. Therefore, characterizing the atherosclerotic plaque components is necessary.

Numerous methods for characterizing the mechanical behaviour of atherosclerotic plaque exist. Uni-axial tensile testing is the frequently used method for determining the mechanical properties of the plaque tissue [21-25] as discussed by Walsh, Cunnane, Mulvihill, Akyildiz, Gijssen and Holzapfel [26]. In addition to stretching due to the pulsatile blood flow, plaque tissue components experience compressive forces. Therefore, compressive tests including stress relaxation [27] micro-indentation [28-30], nano-indentation [31,32] were also used for the plaque characterization.

Vibrational spectroscopy is a potential method for the investigation of biological tissues. FTIR microspectroscopy is a non-destructive analytical vibrational spectroscopy technique used for the identification of chemical and structural information within the tissue specimens [33-35]. FTIR microspectroscopy visually demonstrates the spatially resolved specific chemical functionalities in the form of heat maps. Several studies have shown the ability of FTIR microspectroscopy to identify different components present within the plaque tissue [36-38]. Therefore, FTIR microspectroscopy imaging is considered as a powerful

technique for the chemical characterization of the biological samples.

Despite, availability of experimental data of the plaque tissue, there are still challenges in developing accurate risk-stratification techniques. Therefore, this study aims to characterize the plaque components structurally (histological analysis) mechanically (Nanoindentation tests) and chemically (Fourier Transform Infrared (FT-IR) microspectroscopy) to enhance understanding regarding the mechanical behaviour of plaque components.

Experimental

Eleven carotid plaques with stenosis > 70%, scheduled for carotid endarterectomy (CEA) in the Princess Alexandra Hospital (PAH), were recruited for this study. This study was approved by the Metro South Human Research Ethics Committee (HREC/17/QPAH/181) and patient content forms were obtained. Immediately after excision, the plaque samples were placed in phosphate buffer solution (PBS) and taken for a low energy X-ray at PAH. Later, the tissue sample was cut into 3-4mm thick segments and placed in aluminium foil cups (made in house) semi-filled with Optimal Cutting Temperature (OCT) compound (Tissue-Tek OCT, TED Pella Inc, CA, USA). Following which, the tissue samples were embedded entirely in OCT, snap frozen using liquid Nitrogen and stored at -20°C within 2h of excision. This method of storage has been used since it has no significant effects on the mechanical properties [31]. To avoid changes in mechanical properties the carotid plaque samples were sectioned using a cryostat (Leica CM1850). The frozen tissue blocks were used for cutting different thickness sections (7µm, 8µm & 30µm). To equilibrate, the frozen block is mounted onto the specimen holder and is kept in a Cryostat maintained at -20°C for 30 mins. Adjacent sections of eight-8µm, one-7µm & and one-30µm thick sections were cut for histology, FTIR and Nano-Indentation respectively. The 8µm and 30µm sections were taken onto the polysine microscope adhesion slides (Thermo Fischer Scientific, USA) which are electrostatically and biochemically adhesive and attracts frozen tissue sections. While the 7µm section is taken onto a Barium Fluoride (BaF₂) substrate [(20mm diameter x 2mm thick polished window) -CRYSTRAN, Core, UK]. Following the sectioning, the polysine glass slides with sections on it were placed in the freezer at -20°C until further experiments. The 7 µm sections taken on BaF₂ substrate were dried for 10 minutes. To remove the OCT few drops of distilled water were placed on the section for 30 seconds. Later the water is carefully removed using a micropipette. The samples were then air-dried for 60 minutes before placing in the freezer at -20°C until further experimentation.

Histology and immunostaining were performed on adjacent sections (8 µm thick). The sections were stained with haematoxylin and eosin (H&E) to identify the basic constituents present in the plaque tissue, Oil Red O (ORO)

for lipids and Masson's trichrome to categorize the fibrous tissue and intra-plaque hemorrhage. Immunostaining was performed to identify the macrophages (CD68- dilution 1:1000) and neovascularization (CD31- dilution 1:1200). For immunostaining (CD68 and CD31), optimization of primary antibodies was done to determine the best dilution for optimal staining. Also, the omission of the primary antibody was used as a negative control, thereby allowing the clarification of degree of non-specific background staining by the secondary antibody (Fig. 1). The histology sections were digitized using a 3D Histech Scan II Fluorescence/Brightfield Slide Scanner (Total magnification 70 x 0.14µm resolution).

Fiji (<https://imagej.net/Fiji/Downloads>) was used to evaluate the staining intensity of H & E, Oil Red O for lipids, Masson's Trichrome for haemorrhage CD68 for inflammation. The percentage staining of lipids, calcification, haemorrhage, and macrophages was reported as the percentage of plaque area calculated from H & E stain. Neovessels were identified from CD31 positive staining that highlights the endothelial cells in the inner lining of the lumen. The number of neovessels was manually counted using a grid of 1 mm². Neovascularization was expressed as neovessels/mm².

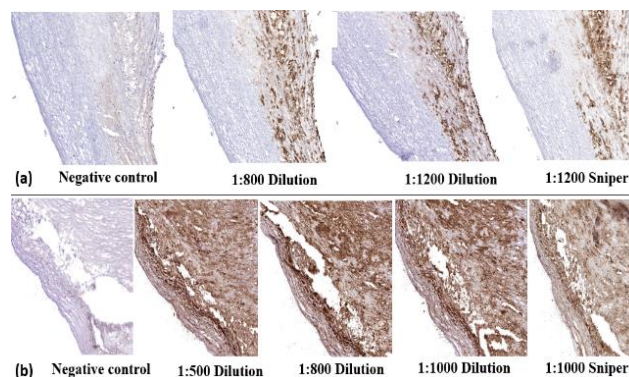


Fig. 1. (a) CD31 negative control (no staining) and different dilutions for selecting optimal staining (1:1200 Sniper); (b) CD68 negative control (no staining) and different dilutions for selecting optimal staining (1:1000 Sniper).

Hysitron TI 950 TriboIndenter was used for the nanomechanical characterization of the tissues. The tests were performed at room temperature using displacement feedback-controlled mode with a normal stage of 5 µm displacement. A conospherical diamond tip, with a radius of curvature of 50 µm, was used for the experiments. This probe is ideal for soft tissue, as the indentation area is much larger at small depths. Therefore, smaller indentation depths can be achieved with this tip. The thickness of the sample being tested is 30 µm, and the depth of penetration is 2000nm, which is 6% of the sample thickness [39]. Accurate tip to optics calibration is vital to ensure the alignment between the centre of the tip and the centre of the visual field. This alignment is desirable for indentation on specific sites, especially for soft tissue characterization. For this reason, dark chocolate was used

to calibrate the 50 μm tip. The schematic of the sample preparation and hydration is shown in **Fig. 2**. A trapezoidal load function consisting of loading, holding and unloading times of 5 s each were applied to the indent site. The maximum displacement of 2000 nm with a constant displacement rate of 400 nm/s was used in this study. [Sample thickness 30 μm].

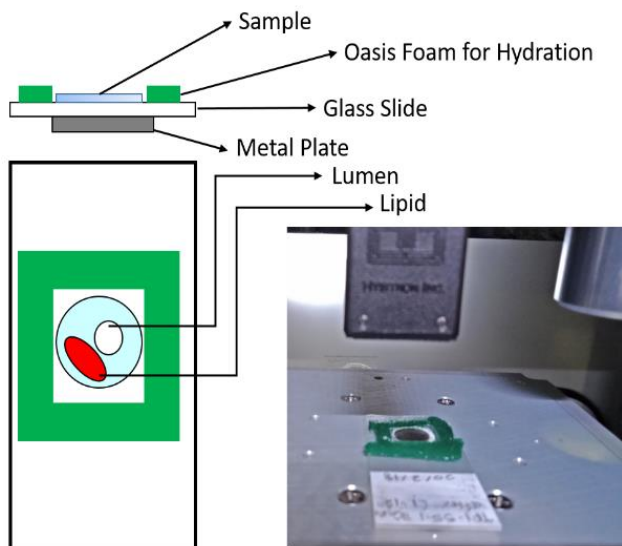


Fig. 2. Schematic of the sample positioning and hydration system for nanoindentation test.

A Nicolet-iS50 FT-IR equipped with a Nicolet continuum microscope was used for the spectral imaging of the carotid plaque tissue [Sample thickness 7 μm]. Histological images were used as the reference to select the areas for FT-IR imaging. All spectra were acquired using transmittance mode with a resolution of 4 cm^{-1} in the wavenumber range between 4000-800 cm^{-1} with 40 x 40 μm^2 aperture area and 64 scan numbers. Due to the large acquisition time of the spectral maps, setting up background scans at regular intervals is essential to account for the variation in atmospheric conditions around the sample. Therefore, background spectra were collected from an area on the BaF2 substrate, which is free of the tissue at every 10-minute interval. This background spectrum was automatically subtracted from the tissue spectra using OMNIC 9 (Thermo Fisher Scientific, Madison, USA). Before the spectral imaging, a visual image of the area was recorded using a continuum microscope.

Results and discussion

Structural characterization

Histological analysis and immunostaining are performed on the sections cut from a segment selected from eleven carotid plaque tissues. It should be noted that the carotid plaque tissue obtained from the hospital is not intact and have some missing part of the tissues. The structural characterization is based on the sections available for

staining. **Fig. 3** represents adjacent sections of a section displaying different morphological characteristics. Analysis of the histological images has shown varied morphology and shape of the lumen (**Table 1**).

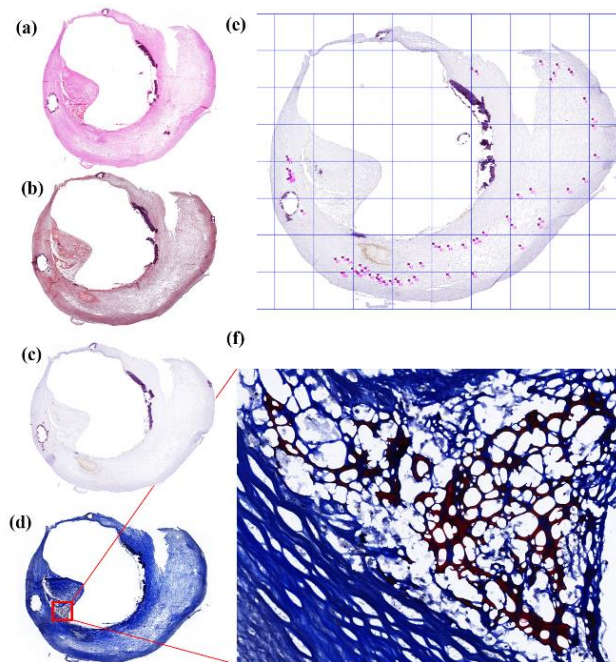


Fig. 3. Example of section representing different staining (a) Haematoxylin Eosin stain; (b) Oil Red O; (c) CD68; (d) Masson's Trichrome; (e) CD31 (neovessels represented by pink dots); (f) Hemorrhage stained in red colour.

Table 1. Summary of the quantitative data extracted from the histological analysis of different patients.

Patient	% LA	% CAL	% HA	%CD68	NV/mm ²
P1	5	0	0	18	1.2
P2	55	1	0	1	0.04
P3	27	6	4	3	2
P4	47	5	4	1	2.01
P5	43	9	0	4	0.75
P6	28	6	0	8	0.56
P7	9	32	8	2	2.57
P8	8	56	0	1	0.55
P9	16	19	0	2	1.47
P10	3	23	5	1	2.06
P11	4	15	1	16	0.67

It was evident that the lipid area (stained in red-Oil Red O staining) and calcification area (Dark pink in H & E) are inversely related **Fig. 4(a)**. Similarly, the % lipid area and % CD68 staining (inflammation- brown colour) were inversely related. Also, % hemorrhage (red in Masson's Trichrome) and neovessels density were positively related (**Fig. 4(b)**). Neovessels density was higher in the sections with hemorrhage. Neovessels were in the shoulder areas, closer to the outer layer of the blood vessel and closer to the locations of the inflammation. In this study, however, no correlation was found between inflammation and microvessels density. It was observed

that the spatial distribution of the neovessels for different patients was associated with the location of inflammation and are closer to the outer wall, similar to previous studies [40].

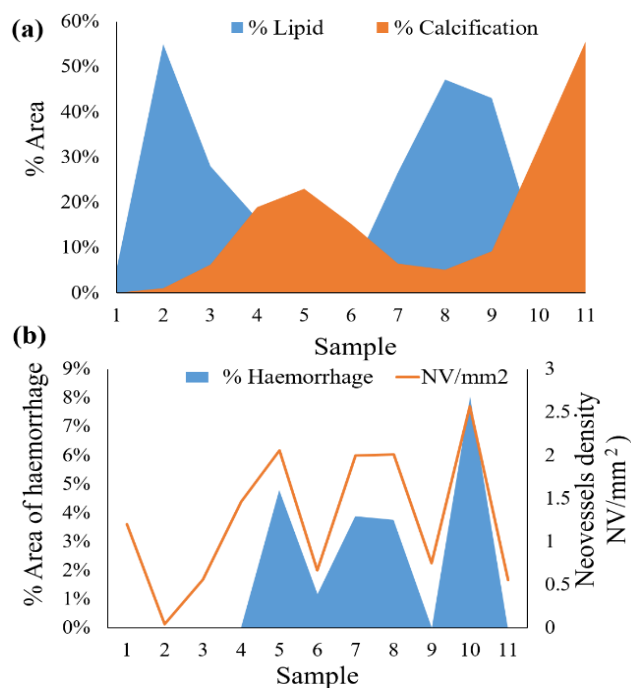


Fig. 4. (a) Relation between % lipid area and % calcification area; (b) Association of haemorrhage and neovessels density.

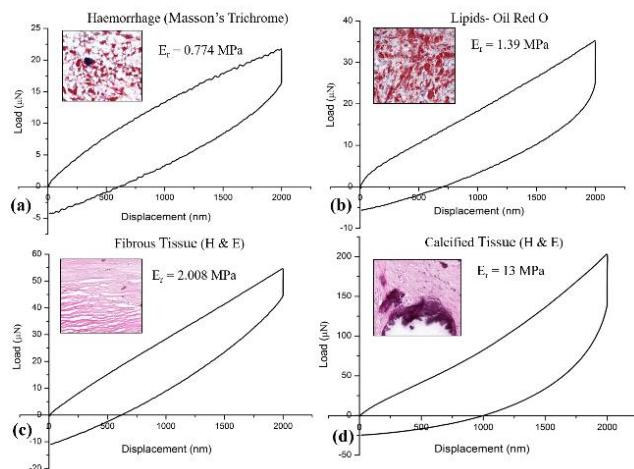


Fig. 5. (a) Load-displacement curves for (a) hematoma; (b) lipid; (c) fibrous tissue; (d) calcified tissue (square indicates the corresponding histological images).

Mechanical characterization

In total, data for 187 indent locations is presented, which excludes the data of indents that were considered incorrect regarding the indentation depth and partial contact of the tip due to loosely structured tissue. The number of indents performed on each section depended on the size of the tissue and structural presentation based on histology. **Fig. 5** represents a tissue section and the corresponding modulus values obtained from nanoindentation test. Indent

locations were selected based on the adjacent histological section and the material properties were sorted based on the tissue type as seen in histological staining. These locations were identified based on the coordinates of the indent position and thereby manually mapped to the locations of the histological section. Based on the locations of indentation, the average modulus values were extracted for each tissue type. The nanoindentation test results (Reduced Modulus) for different patients were presented in **Table 2**.

Table 2. Patient-specific reduced modulus values for different tissues.

Patient	Fibrous	Lipid	Calcified	Partially Calcified
1	2.2085	1.279667		
2	2.605118	1.293	9.533	3.441
3	1.4775	0.636	20.368	
4	2.8238	0.8225	109.312	3.36
5	2.15675	1.238714	6.779714	3.921
6	2.056714	1.308333	14.43867	2.796
7	1.380818		5.235333	3.6002
8	5.3231	1.06	9.8964	
9	2.55		42.67	3.36
10	3.466	1.06	17.4764	2.129
11	2.024813	1.2252	6.2865	3.36

The properties of calcification were influenced by the density at the site of indentation. It must be noted that a part of calcium content is lost during the sample preparation phase. There were no correlations found between the locations or patients analysed in this study. The values varied between tissue types, and there were differences in the same tissue. The reduced modulus values for the fibrous tissues were influenced by the compositional changes. The reduced modulus was high for structured collagen regions compared to the unstructured collagen regions [29]. The mean reduced modulus values obtained for different tissue types are consistent with a higher range of values obtained in the literature [41]. The patient-specific average values for each tissue type were defined for the 2D structural simulations. The heterogeneous nature of the atherosclerotic plaque tissue can be determined by the comprehensive mapping of the material properties in the submicron level, which has further challenges. This mapping might provide more insights regarding the stress distribution and stress concentration locations.

Chemical characterization

FTIR Microspectroscopy mapping of the carotid plaque tissue was performed on the unstained 7 μm thick sections placed on BaF₂ windows. The region for microspectroscopy was identified based on the adjacent histological sections. The time duration for the acquisition of FTIR micro spectra depended on the size of the photomicrograph defined. The histological section, photomicrograph, and corresponding chemical images for

the lipid, fibrous tissue, mineral content and the FTIR absorption spectra of a section at location shows by the cross mark (red colour) in (c) are shown in Fig. 6. The chemical image is based on the absorbance of IR radiation and vibrations of the moieties within the molecules. The prominent peaks found in the FTIR spectra include the amide, lipid and mineral peaks. The main constituents of the vascular tissue comprise of proteins such as collagen and elastin and are attributed to amide I (1665 cm^{-1}), II (1538 cm^{-1}) and III (1238 cm^{-1}) peaks. The two peaks at 2922 cm^{-1} and 2851 cm^{-1} corresponds to the lipids, and the peak at 1736 cm^{-1} corresponds to the lipid esters. The mineral content is attributed to the phosphorous peak at 1083 cm^{-1} .

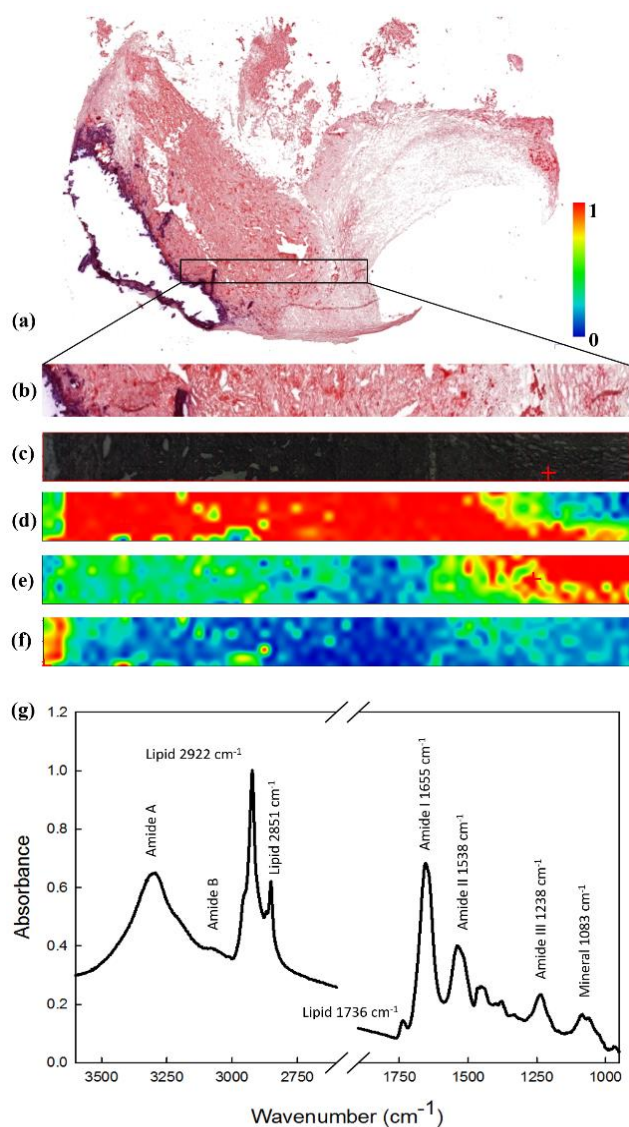


Fig. 6. FTIR Microspectroscopy mapping (a) Reference histological section; (b) Region selected for the acquisition of spectra; (c) Photomicrograph of the region of a section; (d) Chemical image corresponding to the presence of lipids; (e) Chemical image corresponding to the presence of fibrous tissue; (f) Chemical image corresponding to the presence of mineral; (g) FTIR spectra of the point shown by the red cross as shown in (c) with peaks representing the absorbance of different tissue types.

The results from this study are consistent with the histological imaging. There was a good correlation between the lipid content, calcification, and fibrous tissue. Apart, from this observation, the FTIR spectra showed the presence of lipid molecules and microcalcification trapped in the complex fibrous structure. Histological analysis also provides detail of the plaque components present. However, for revealing each component, different staining is required. Whereas, FTIR microspectroscopy mapping presents the chemical composition of all the components present in a single map. This mapping might be helpful in future to assign the component-specific mechanical properties for accurate finite element analysis. However, current studies for mapping the chemical composition of the whole section using FTIR microspectroscopy require long testing durations. Thus, future studies for mapping the chemical composition of the whole section are required.

Limitations

Despite extensive optimization, there are limitations which require further research. Firstly, the tissue sample was slit longitudinally during CEA. Therefore, the shape of the histology image was out of its original shape. Also, only one slice is analyzed from each sample. Secondly, the reduced modulus values have been influenced by the substrate effects at locations where there are gaps in the tissue due to the loss of calcification or lipids during sample preparation as visible from histology. Moreover, nanoindentation tests take longer duration. Therefore, to minimize the degradation of the samples, a suitable fluid medium maintained at physiological temperature is required. In this study, the samples are hydrated with PBS and are tested at room temperature. Also, a fluid tip would be appropriate for testing the samples, as the challenge of maintaining the sample hydration would be eliminated. However, it should be noted that finding the sample would be a challenge.

In this study, the reduced modulus was calculated by using the hertz contact mechanics which assumes the structural homogeneity. Further studies must consider more complex methodology to capture the heterogeneity of the plaque tissue. Since the nanoindentation technique enables measurement in the sub-micron level, tissue-specific material properties have been identified by mapping the locations with the histological sections. Future study will develop accurate mapping techniques with more indent locations to capture the heterogeneity of the tissue.

Furthermore, to have a negligible substrate effect and compensate for any surface roughness issues, it might be appropriate to use cyclical trapezoidal loading protocols for varying displacement depths. The complex nature of the plaque tissue needs more research enabling the mapping of the tissue properties at the sub-micron level. Another limitation is the current studies for mapping the chemical composition of the whole section using FTIR microspectroscopy requires long testing durations. Thus,

future studies for mapping the chemical composition of the whole section are required. This mapping will aid us in developing accurate material models for the biomechanical analysis.

Conclusion

Histological analysis, nanoindentation and FTIR microspectroscopy were utilized to investigate the structural, mechanical properties and composition for atherosclerotic plaque tissue. The biological content and composition of human atherosclerotic plaque tissue have been shown to significantly influence the mechanical response of samples. This is demonstrated by the changes in mechanical behaviour due to increasing calcification. Significant differences are identified in the mechanical properties and composition of plaque tissue in a sample at different locations thereby demonstrating the heterogeneous and complex structure of the tissue. Histology and MRI segmentation are found to have good correlation. This data represents a step towards an enhanced understanding of the mechanical properties of the human atherosclerotic plaque. Besides, large scale studies on the mechanical properties and patient-specific computational simulations are required to develop a risk stratification technique for the vulnerability assessment of the plaque.

Acknowledgements

This work was supported by the Queensland University of Technology (QUT), the Australian Research Council (ARC) [FT140101152 and DP180103009] and the PA Research Foundation (PARF). The authors would like to thank the team at PA Hospital for identifying potential research participants, obtaining patient consent, and providing facilities for a low energy X-ray (Gillian Jagger, Dr Thomas Lloyd, Dr Tim McGahan). The authors would also like to acknowledge the technical support of QUT's Institute of Health and Biomedical Innovation (IHBI) histology facility and Central Research Analytical facility (CARF).

Author's contributions

The work was designed by PKP, PKDVY, YT and ZL. Histological analysis was performed by PKP, TY. Nanoindentation experiments were performed by PKP. Data Analysis was performed by PKP, JBM and JW. PKP wrote the manuscript text. All authors reviewed the manuscript.

Keywords

Atherosclerotic plaque, nanoindentation, FTIR microspectroscopy, Immunostaining.

Received: 13 January 2020

Revised: 15 March 2020

Accepted: 16 March 2020

References

1. Morbiducci, U.; Kok, A.M.; Kwak, B.R.; Stone, P.H.; Steinman, D.A.; Wentzel, J.J.; *Thrombosis and Haemostasis*, **2016**, *115*, 484.
2. Ross, R.; *Nature*, **1993**, *362*, 801.
3. Insull, W.; *The American Journal of Medicine*, **2009**, *122*, S3.
4. Levy, E.I.; Mocco, J.; Samuelson, R.M.; Ecker, R.D.; Jahromi, B.S.; L.N. Hopkins, *Journal of the American College of Cardiology*, **2008**, *51*, 979.
5. Benjamin, E.J.; Virani, S.S.; Callaway, C.W.; Chamberlain, A.M.; Chang, A.R.; Cheng, S.; Chiuve, S.E.; Cushman, M.; Dellinger, F.N.; Deo, R.; Ferranti, S.D.d.; Ferguson, J.F.; Fornage, M.; Gillespie, C.; Isasi, C.R.; Jiménez, M.C.; Jordan, L.C.; Judd, S.E.; Lackland, D.; Lichtman, J.H.; Lisabeth, L.; Liu, S.; Longenecker, C.T.; Lutsey, P.L.; Mackey, J.S.; Matchar, D.B.; Matsushita, K.; Mussolino, M.E.; Nasir, K.; O'Flaherty, M.; Palaniappan, L.P.; Pandey, A.; Pandey, D.K.; Reeves, M.J.; Ritchey, M.D.; Rodriguez, C.J.; Roth, G.A.; Rosamond, W.D.; Sampson, U.K.A.; Satou, G.M.; Shah, S.H.; Spartano, N.L.; Tirschwell, D.L.; Tsao, C.W.; Voeks, J.H.; Willey, J.Z.; Wilkins, J.T.; Wu, J.H.; Alger, H.M.; Wong, S.S.; Muntner, P.; *Circulation*, **2018**, *137*, e67.
6. Finn, A.V.; Nakano, M.; Narula, J.; Kolodgie, F.D.; Virmani, R.; *Arteriosclerosis Thrombosis and Vascular Biology*, **2010**, *30*, 1282.
7. Narula, J.; Garg, P.; Achenbach, S.; Motoyama, S.; Virmani, R.; Strauss, H.W.; *Nature Clinical Practice Cardiovascular Medicine*, **2008**, *5*(SUPPL. 2).
8. Vancraeynest, D.; Pasquet, A.; Roelants, V.; Gerber, B.L.; Vanoverschelde, J.L.J.; *Journal of the American College of Cardiology*, **2011**, *57*, 1961.
9. Makris, G.C.; Teng, Z.; Patterson, A.J.; Lin, J.M.; Young, V.; Graves, M.J.; Gillard, J.H.; *British Journal of Radiology*, **2015**, *88*, 1052.
10. Trivedi, R.A.; Gillard, J.H.; Kirkpatrick, P.J.; *British Journal of Neurosurgery*, **2008**, *22*, 350.
11. Gao, H.; Long, Q.; Das, S.K.; Sadat, U.; Graves, M.; Gillard, J.H.; Li, Z.Y.; *Annals of Biomedical Engineering*, **2011**, *39*, 2203.
12. Paritala, P.K.; Yarlalagadda, P.K.D.V.; Wang, J.; Gu, Y.; Li, Z.; *Engineering Fracture Mechanics*, **2018**, *204*, 531.
13. Huang, Y.; Teng, Z.; Sadat, U.; Graves, M.J.; Bennett, M.R.; Gillard, J.H.; *Journal of Biomechanics*, **2014**, *47*, 1465.
14. Li, Z.Y.; Taviani, V.; Gillard, J.H.; 30th Annual International Conference of the IEEE Engineering in Medicine and Biology Society, IEEE, **2008**, pp. 1373-1376.
15. Holzapfel, G.A.; Mulvihill, J.J.; Cunnane, E.M.; Walsh, M.T.; *Journal of Biomechanics*, **2014**, *47*, 859.
16. Teng, Z.; He, J.; Degnan, A.J.; Chen, S.; Sadat, U.; Bahaei, N.S.; Rudd, J.H.F.; Gillard, J.H.; *Atherosclerosis*, **2012**, *223*, 321.
17. Tang, D.; Yang, C.; Zheng, J.; Woodard, P.K.; Saffitz, J.E.; Sicard, G.A.; Pilgram, T.K.; Yuan, C.; *Journal of Biomechanical Engineering*, **2005**, *127*, 1185.
18. Akyildiz, A.C.; Speelman, L.; Nieuwstadt, H.A.; van Brummelen, H.; Virmani, R.; van der Lugt, A.; van der Steen, A.F.W.; Wentzel, J.J.; Gijssen, F.J.H.; *Computer Methods in Biomechanics and Biomedical Engineering*, **2016**, *19*, 771.
19. Taylor, C.A.; Figueroa, C.A.; *Annual Review of Biomedical Engineering*, **2009**, pp. 109-134.
20. Gao, H.; Long, Q.; Graves, M.; Gillard, J.H.; Li, Z.Y.; *Journal of Biomechanics*, **2009**, *42*, 1416.
21. Holzapfel, G.A.; Sommer, G.; Regitnig, P.; *Journal of Biomechanical Engineering*, **2004**, *126*, 657.
22. Davis, L.A.; Stewart, S.E.; Carsten Iii, C.G.; Snyder, B.A.; Sutton, M.A.; Lessner, S.M.; *Acta Biomaterialia*, **2016**, *43*, 101.
23. Cunnane, E.M.; Mulvihill, J.J.E.; Barrett, H.E.; Hennessy, M.M.; Kavanagh, E.G.; Walsh, M.T.; *Journal of Biomechanics*, **2016**, *49*, 3697.
24. Barrett, H.E.; Cunnane, E.M.; Kavanagh, E.G.; Walsh, M.T.; *Journal of the Mechanical Behavior of Biomedical Materials*, **2016**, *56*, 45.
25. Teng, Z.; Feng, J.; Zhang, Y.; Sutcliffe, M.P.F.; Huang, Y.; Brown, A.; Jing, Z.; Lu, Q.; Gillard, J.; *Journal of Biomechanics*, **2015**, *3859*.
26. Walsh, M.T.; Cunnane, E.M.; Mulvihill, J.J.; Akyildiz, A.C.; Gijssen, F.J.H.; Holzapfel, G.A.; *Journal of Biomechanics*, **2014**, *47*, 793.
27. Salunke, N.V.; Topoleski, L.D.T.; Humphrey, J.D.; Mergner, W.J.; *Journal of Biomedical Materials Research*, **2001**, *55*, 236.
28. Barrett, S.R.H.; Sutcliffe, M.P.F.; Howarth, S.; Li, Z.Y.; Gillard, J.H.; *Journal of Biomechanics*, **2009**, *42*, 1650.
29. Chai, C.K.; Akyildiz, A.C.; Speelman, L.; Gijssen, F.J.H.; Oomens, C.W.J.; van Sambeek, M.R.H.M.; van der Lugt, A.; Baaijens, F.P.T.; *Journal of Biomechanics*, **2013**, *46*, 1759.
30. Chai, C.K.; Speelman, L.; Oomens, C.W.J.; Baaijens, F.P.T.; *Journal of Biomechanics*, **2014**, *47*, 784.

31. Ebenstein, D.M.; Coughlin, D.; Chapman, J.; Li, C.; Pruitt, L.A.; *Journal of Biomedical Materials Research Part A*, **2009**, *91A(4)*, 1028.
32. Cahalane, R.M.; Barrett, H.E.; O'Brien, J.M.; Kavanagh, E.G.; Moloney, M.A.; Walsh, M.T.; *Acta Biomaterialia*, **2018**, *80*, 228.
33. Kumar, S.; Chaudhary, S.; Jain, D.C.; *Open Journal of Applied Sciences*, **2014**, *4(03)*, 103.
34. Marzec, K.M.; Wróbel, T.P.; Fedorowicz, A.; Mateuszuk, Ł.; Maślak, E.; Jaształ, A.; Chlopicki, S.; *Optical Spectroscopy and Computational Methods in Biology and Medicine*, Springer, **2014**, pp. 505-535.
35. Orsini, F.; Ami, D.; Villa, A.M.; Sala, G.; Bellotti, M.G.; Doglia, S.M.; *Journal of Microbiological Methods*, **2000**, *42*, 17.
36. Manoharan, R.; Baraga, J.J.; Rava, R.P.; Dasari, R.R.; Fitzmaurice, M.; Feld, M.S.; *Atherosclerosis*, **1993**, *103*, 181.
37. Palombo, F.; Shen, H.; Benguigui, L.E.S.; Kazarian, S.G.; Upmacis, R.K.; *Analyst*, **2009**, *134*, 1107.
38. Wrobel, T.P.; Mateuszuk, L.; Chlopicki, S.; Malek, K.; Baranska, M.; *Analyst*, **2011**, *136*, 5247.
39. Fischer-Cripps, A.C.; *Vacuum*, **2000**, *58*, 569.
40. Taqueti, V.R.; Di Carli, M.F.; Jerosch-Herold, M.; Sukhova, G.K.; Murthy, V.L.; Folco, E.J.; Kwong, R.Y.; Ozaki, C.K.; Belkin, M.; Nahrendorf, M.; Weissleder, R.; Libby, P.; *Circulation: Cardiovascular Imaging*, **2014**, *7*, 920.
41. Ebenstein, D.M.; Chapman, J.M.; Li, C.; Saloner, D.; Rapp, J.; Pruitt, L.A.; *MRS Online Proceedings Library Archive*, **2001**, 711.